PUBLICATIONS OF THE ASTRONOMICAL SOCIETY OF THE PACIFIC, **119**: 303–317, 2007 March

A Subsystem Test Bed for the Frequency-Agile Solar Radiotelescope

ZHIWEI LIU, DALE E. GARY, AND GELU M. NITA

Center for Solar-Terrestrial Research, New Jersey Institute of Technology, Newark, NJ

STEPHEN M. WHITE

Department of Astronomy, University of Maryland, College Park, MD

AND

GORDON J. HURFORD

Space Science Laboratory, University of California, Berkeley, CA

Received 2006 December 22; accepted 2007 January 17; published 2007 March 2

ABSTRACT. This paper describes the design and operation of the Frequency-Agile Solar Radiotelescope (FASR) Subsystem Testbed (FST) and the first observational results. Three antennas of the Owens Valley Solar Array have been modified so that each sends a 1–9 GHz band of radio frequency to a central location using a broadband analog optical fiber link. A dynamically selected 500 MHz subset of this frequency range is digitized at 1 Gsps (gigasample per second) and recorded to disk. The full-resolution time-domain data thus recorded are then correlated through offline software to provide interferometric phase and amplitude spectra on three baselines. An important feature of this approach is that the data can be reanalyzed multiple times with different digital signal-processing techniques (e.g., different bit-sampling, windowing, and radio frequency interference [RFI] excision methods) to test the effect of different designs. As a prototype of the FASR system, FST provides the opportunity to study the design, calibration, and interference-avoidance requirements of FASR. In addition, FST provides, for the first time, the ability to perform broadband spectroscopy of the Sun with spectrograph-like spectral and temporal resolution, while providing locating ability for simple sources. Initial observations of local RFI, geostationary satellite signals, global positioning system (GPS) satellite signals, and the Sun are presented to illustrate the system performance.

1. INTRODUCTION

Observations of radio emission associated with solar flares provide diagnostics for flare physics, origin of coronal mass ejections, particle acceleration and propagation, and coronal heating. Historically, two approaches to solar observations have been imaging observations at a few discrete frequencies, and spectroscopy without spatial resolution. Imaging (interferometric) arrays have been implemented at discrete frequencies, such as the Very Large Array (VLA; US; 0.075, 0.3, 1.4, 5, 8.5, 15, and 23 GHz; Napier et al. 1983), the Nobeyama Radioheliograph (Japan; 17 and 34 GHz; Nakajima et al. 1994), and the Nancay Radioheliograph (France; 150, 164, 237, 327, and 410 MHz; Kerdraon & Delouis 1997). Interferometers require a large number of antennas for good UV plane coverage and high angular resolution. Broadband high-frequency-resolution spectroscopy, on the other hand, usually exploits swept-frequency or broadband digital spectrographs, such as those at Zurich (Switzerland; 0.1–4 GHz; Messmer et al. 1999), Nancay (France; 20–70 MHz; Lecacheux 2000), Culgoora (Australia; 18–1800 MHz; Prestage et al. 1994), and Green Bank (US; 12–1000 MHz; Bastian et al. 2005). Two radio facilities with simultaneous spatial and spectral resolution are RATAN 600 (Russia; 1–20 GHz; Bogod et al. 1999) and Owens Valley Solar Array (OVSA; US; 1–18 GHz; Hurford et al. 1984), but neither have the image quality necessary to fully exploit the diagnostic potential of radio emission from the Sun. For this, both imaging and spectroscopy data must be obtained simultaneously over a large bandwidth, with angular, time, and spectral resolution corresponding to the properties intrinsic to solar radio emissions. The solar-dedicated Frequency-Agile Solar Radiotelescope (FASR) was proposed to meet the challenge (Bastian 2003).

FASR represents a major advance over existing solar radio telescopes and is expected to remain the world's premier solar radio instrument for 2 decades or more after completion. It will use hundreds of antennas to perform broadband imaging spectroscopy over a frequency range of 0.05–20 GHz, with spatial, spectral, and temporal resolutions that are designed to exploit radio diagnostics of the wide variety of physical processes that occur in the solar atmosphere (Gary & Keller 2004). To construct a prototype and characterize the broadband radio frequency (RF) transmission system and digital signal processing to be used for FASR, we have developed the FASR Subsystem Testbed (FST).

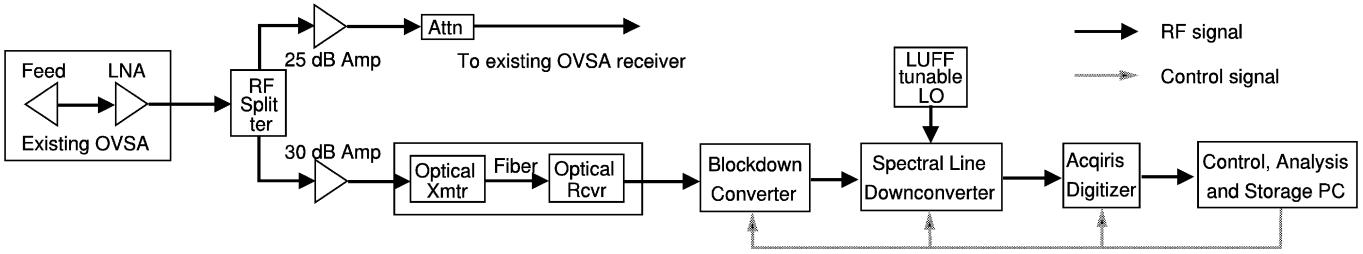

FIG. 1.—Block diagram of one channel of the FASR subsystem test bed. The signal is split to feed the OVSA receiver and FST optical links simultaneously, so there is no impact on OVSA's operation.

As a test bed for the FASR system, FST provides the opportunity to study the design, calibration, and radio frequency interference (RFI) mitigation requirements for FASR. FST is also the first system with the ability to combine Nyquist-limited high time and frequency resolution with the interferometric ability to locate sources. The design and operation of the FST system are outlined in § 2. First results of geostationary satellite, global positioning system (GPS) satellite, and solar observations are described in § 3. Finally, a summary and conclusion are given in § 4.

2. DESIGN AND DEVELOPMENT

As a partial prototype for FASR, FST is far more modest than FASR in terms of performance. Its goal is to provide a platform for the study of the design of some elements of the FASR RF and signal-processing system, as well as approaches to calibration and RFI excision for FASR. The basic idea of FST is to return broadband RF to the control room, where all subsequent signal processing can be done. It is anticipated that FASR will use this general approach, which provides a highly flexible design with minimal hardware (and associated self-generated RFI) in the field. For FST, the RF is down-converted in the control room to a single-sideband intermediate frequency (IF) with a 500 MHz bandwidth, which is digitized and recorded as digital data at an 8 bit amplitude resolution and full frequency resolution. Such data can then be digitally processed offline with alternate algorithms, including down-sampling, channelization via polyphase filters or other methods, RFI detection and excision, and correlation. As the various approaches to digital signal processing for FASR are being contemplated, we can implement each one in the software and quantitatively investigate its performance with FST, using data recorded under actual solar and RFI observing conditions.

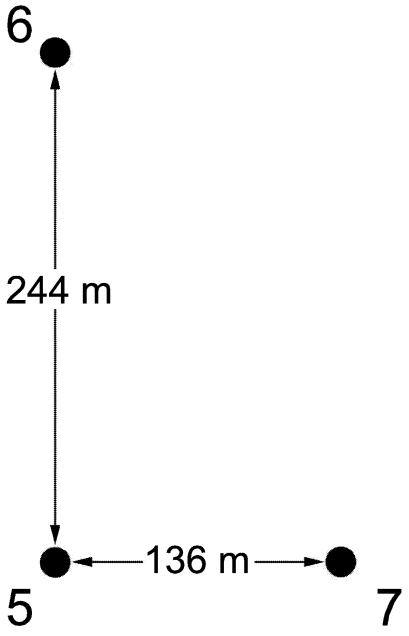

FIG. 2.—Antenna configuration of the FASR subsystem test bed (1.8 m antennas; Nos. 5, 6, and 7 of the OVSA). The longest baseline is 280 m in this nearly right-triangle configuration.

2.1. System Configuration

Figure 1 shows a block diagram overview of one channel of the FST system and its relationship to the existing OVSA infrastructure. The OVSA (Hurford et al. 1984) is a solar-dedicated interferometric array that takes daily observations roughly covering the time range 16:00–24:00 UT. After undergoing some upgrades (Gary & Hurford 1999), the array now consists of two 27 m antennas and five 1.8 m antennas that can observe the Sun at up to 86 frequencies in the range 1–18 GHz. For FST, we used three of the seven existing OVSA antennas, choosing antennas 5, 6, and 7—three identical 1.8 m antennas arranged in a nearly right triangle (shown in Fig. 2). The longest baseline is 280 m. The output of the front-ends of antennas 5, 6, and 7 are split to simultaneously feed the OVSA receivers and FST. Thus, there is no impact on OVSA's normal operation, and we can also use the existing antenna pointing and tracking system. The OVSA RF is amplified by 25 dB and then attenuated by 20 dB to isolate the OVSA signal path from the FST path. After the power divider, the FST signals are amplified by 30 dB and sent via broadband (11 GHz) RF optical links (link gain −30 dB; the same links are used for the Allen Telescope Array [DeBoer 2004]). The

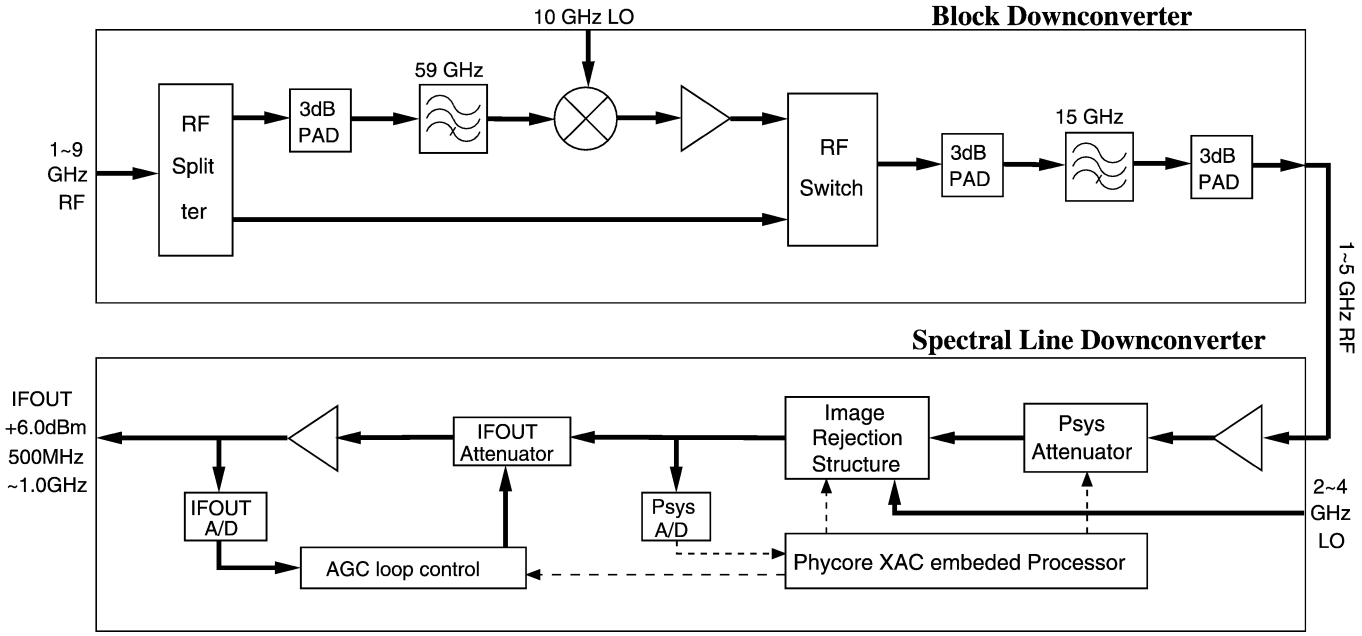

FIG. 3.—Two stages of down-conversion: block (*top*) and spectral line (*bottom*). The digitizer performs an implicit third stage of down-conversion, due to its sampling below the Nyquist frequency.

direct-burial hybrid-fiber cable (Corning ALTOS armored cable) from each antenna is composed of three single-mode fibers (one used for the RF, and two spares) and three multimode fibers (for future use). The cable lengths from antennas 5 and 7 are precisely matched (232.9 m), while the length from antenna 6 is longer (402.0 m). This allows us to investigate how thermal changes in the fiber affect phase stability, since such effects should be minimal on the matched baseline 5–7 and have a precisely opposite behavior on baselines 5–6 and 6–7.

Because the RF is transmitted to the control room before any RF down-conversion, it is not necessary to provide separate phase locking during down-conversion; the local oscillator (LO) signal from a single source can be distributed to each of the mixers directly. The task of converting the broadband RF to a single-sideband IF signal suitable for digitizing is accomplished in two stages, as shown in Figure 3. First, the RF from each antenna is block down-converted (§ 2.2) to a 1–5 GHz RF that is switchable over the 1–9 GHz range. The 1–5 GHz signal is then input into a spectral-line down-converter module (§ 2.3) designed for the CARMA array (Bock et al. 2006) in order to produce a single-sideband, 500 MHz bandwidth IF that is tunable anywhere over the 1–5 GHz band. The single-sideband IF is digitized at 1 Gsps (gigasample per second) and transferred to a hard disk for storage (§ 2.4) and postprocessing (§ 2.6).

2.2. Down-Converter

The 1–9 GHz broadband spectrum is split into two 4 GHz wide channels, as shown in Figure 3. Channel 1 goes directly to the two-way switch, while channel 2 goes to a 10 GHz mixer. The LO signal is provided by a 10 GHz phase-locked oscillator (Herley-CTI XPDRO) fed by a 10 MHz reference provided by a rubidium frequency standard (Stanford Research Systems PRS10). The mixer output, after filtering, is the difference of the LO frequency and the incident RF spectrum, and hence it inverts the spectrum over the 5 GHz frequency point. Thus, after the 1–5 GHz bandpass filter, channel 1 is the lower 1–5 GHz band, and channel 2 is the upper 1–5 GHz band (containing the 9–5 GHz RF). The upper and lower bands are selected by means of an RF switch in response to a control signal from the control PC. We refer to the two 1–5 GHz channels as the "upper band" and "lower band" in order to differentiate from the similar "upper sideband" and "lower sideband" provided by the spectral-line down-converter.

2.3. Spectral-Line Down-Converter

The selected 1–5 GHz band from each channel is input to each of the three spectral-line down-converter modules (see Fig. 3, *bottom*) to produce a single-sideband IF with a 500 MHz bandwidth (ranging from 500 to 1000 MHz), which is tunable anywhere within the 1–5 GHz band. The tunable LO is provided by a frequency synthesizer composed of a 10 MHz reference (provided by the same rubidium frequency standard as above) and a tunable oscillator (Luff Research), which can be locked to a frequency between 2 and 4 GHz in 20 MHz steps. The FST system uses only the 2, 2.5, 3, 3.5, and 4 GHz LO settings. The tunable oscillator's frequency-switching speed is <2 ms.

The frequency range of the selected 500 MHz bandwidth is determined by the band B, sideband S, and LO frequency $\nu_{\rm LO}$ parameters, according to

$$\nu_{\rm base} = \sigma[10{,}000(1 - B)(1 - 2S) - \nu_{\rm LO}(1 - 2S) - 1000] \quad (1)$$

where the unit is MHz, $B = 0$ and 1 for 5–9 and 1–5 GHz, respectively, $S = 0$ and 1 for the upper and lower sideband of the LO, respectively, and σ is a parameter that determines whether the frequency order is inverted: $\sigma = 1$ if $B = S$, $\sigma = -1$ otherwise. The frequency range observed then ranges from $\nu_{\rm base}$ to $\nu_{\rm base} + 500\ \sigma$.

The spectral-line down-converter module can be divided into the RF signal-processing, automatic gain control (AGC), and card control functions (Fig. 3). The 1–5 GHz signal that goes into the RF part passes through a Hartley image rejection architecture, which provides at least 25 dB rejection of the image signal to yield a single-sideband 500 MHz bandwidth signal (500–1000 MHz). The variable-voltage AGC maintains a fixed output power level of 6 dBm, optimum for the following digitizer. The card control includes the power supply, the CANbus card, and the embedded CPU PHYCore-XAC module needed to control the down-converter module, which communicates with the control PC through the CAN (controller area network) bus. In order to suppress the image frequency, the standard Hartley image rejection architecture (Hartley 1928) is used. The incoming RF signal is divided into I and Q channels and is mixed with a quadrature phase signal, $\cos(\omega_{\rm LO}t)$ and $\sin(\omega_{\rm LO}t)$, derived from the LO. The resulting signals are low-pass filtered, and the Q-channel (I-channel) signal is shifted by 90° (−90°) before final summation of the two channels. The choice of which sideband will be suppressed is software programmable through a CANbus message.

This module has two levels of attenuation, $P_{\rm sys}$ and $\rm IF_{out}$ attenuation, each having an attenuation range from 0 to 31.5 dB. $P_{\rm sys}$ attenuation must be manually adjusted according to the incoming signal power level by resetting the board or by sending a $P_{\rm sys}$ level-set command. Once set, this level is held fixed. Its purpose is to keep the signal coming into the AGC loop in the middle of the $\rm IF_{out}$ attenuation range (~15 dB). In contrast, the $\rm IF_{out}$ attenuation is changed dynamically by the AGC to keep the output power level at 6 dBm. The digitized samples are scaled to total power by applying the measured $P_{\rm sys}$ power level, adjusted for the current value of $P_{\rm sys}$ attenuation. $P_{\rm sys}$ is the signal power level right before the AGC loop, and is measured every 100 ms and broadcast in CANbus "monitor packets" (five measurements arrive every 0.5 s). Each 0.5 s set of monitor packets also contains one measurement of the current value of $\rm IF_{out}$, with which we can verify that the signal is in range (i.e., that $\rm IF_{out}$ is 6 dBm).

2.4. Digitization and Storage

The 500–1000 MHz output of each of the three spectral-line down-converters is digitized using an 8 bit, 1 Gsps digitizer (composed of a four-channel Acqiris DC271 digitizer with 2 Mbyte per channel onboard memory, although only three channels are needed). By the Nyquist theorem, the sampled digital signal frequency ranges from 0 to 500 MHz. The total 6 Mbyte of data for three channels is transferred to the PC memory and then to a SATA (serial advanced technology attachment, or serial ATA) hard disk at speeds better than 40 Mbytes $\rm s^{-1}$. Using two independent computational threads, once the transfer to PC memory is complete, a new acquisition can be started and transferred while another thread writes the previously transferred data to the disk. The new acquisition typically finishes before the data-writing is complete, and the two loops are synchronized by pausing the acquisition and transfer thread until the writing thread is ready. This sequence runs continuously with a duty cycle near 1%. Figure 4 (*top*) shows the timing of the digitizer and recording system when operating in this mode.

In many cases, it is desirable to avoid the long time gaps of the order of 200 ms between data acquisitions. As an alternative to filling up the 2 Mbyte onboard memory in one continuous acquisition, the digitizer can operate in a sequence acquisition mode (mode 2, as shown in Fig. 4, *middle*). In sequence acquisition mode, the acquisition memory is divided into a preselected number of segments. The waveforms are stored in successive memory segments as they arrive, until the 2 Mpoint per channel memory is filled (e.g., 20 segments of 100 kpoints each). In this mode, each waveform requires its own individual trigger, and the trigger delay time is controllable. This allows us to smooth out the time gaps, and although the duty cycle does not improve, the time sampling becomes more regular. In this mode, the timing of the waveforms is precisely controlled within an acquisition, with a variable time gap between acquisitions, as shown in the figure.

A third useful mode (a trivial modification to mode 1) is shown in Figure 4 (*bottom*). Here we simply reduce the number of points in an acquisition, thereby also reducing the transfer time. By taking 100 kpoints, the system can transfer and write the data and be ready for a new acquisition in as little as 12.5 ms. To limit the data volume, one can lengthen the cycle time. The timing is then similar to mode 2 but avoids the longer (165 ms) time gaps due to data transfer. The disadvantage with respect to mode 2 is that the time between samples is not precisely controlled. Figure 5 shows the typical timing between acquisitions in mode 3 for a nominal cycle time of 20 ms.

2.5. Control System and Data Structure

The cooperation of the different modules of the system requires the development of a control system. The antenna pointing is controlled by the existing OVSA control system, so pointing to calibration sources and communication satellites,

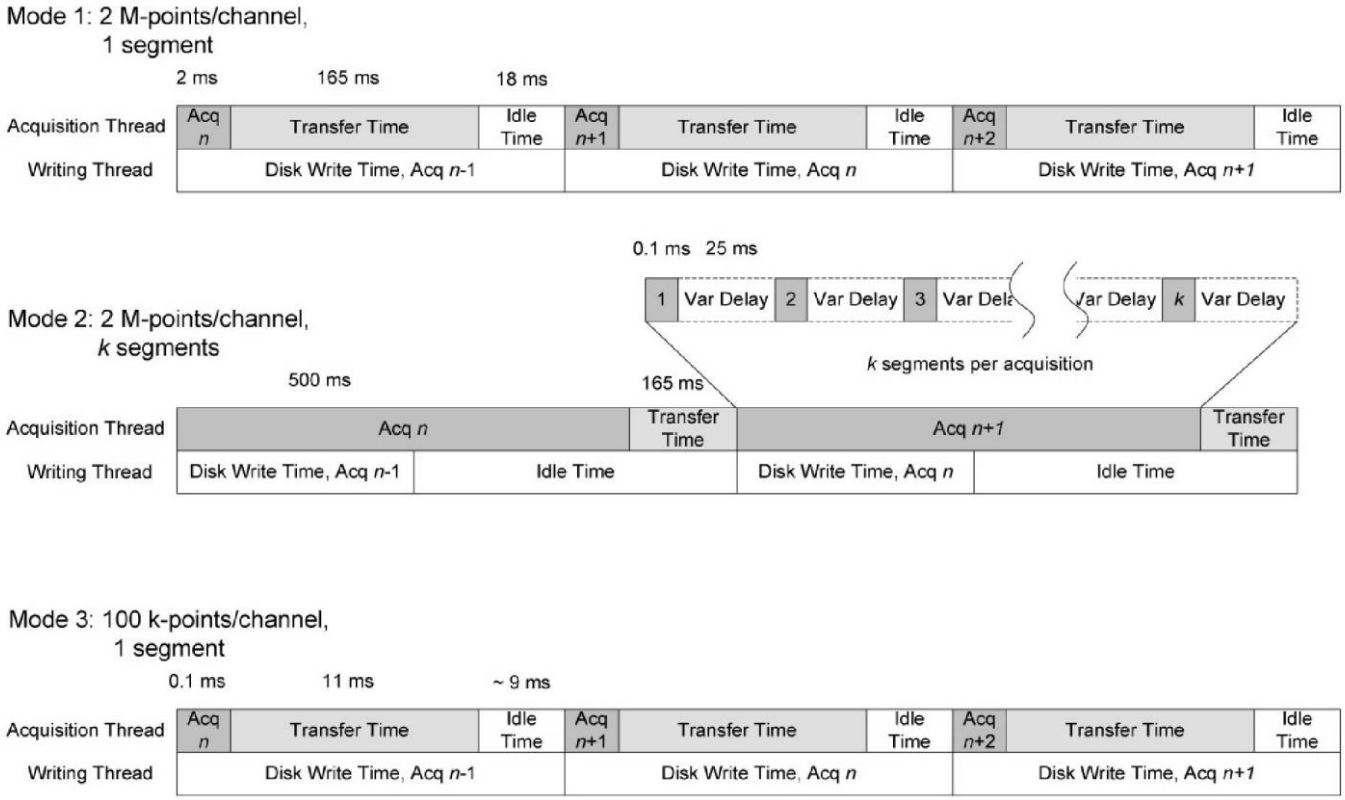

FIG. 4.—Timing diagram of acquisition (*dark gray*), data transfer *(light gray*), and data recording (*white*) for the three most commonly used modes of digitizer operation. The acquisition/data transfer and disk-writing tasks are implemented as two independent execution threads. The typical times for each task, as actually used by us, are shown above each acquisition thread. In mode 2, we typically use $k = 20$.

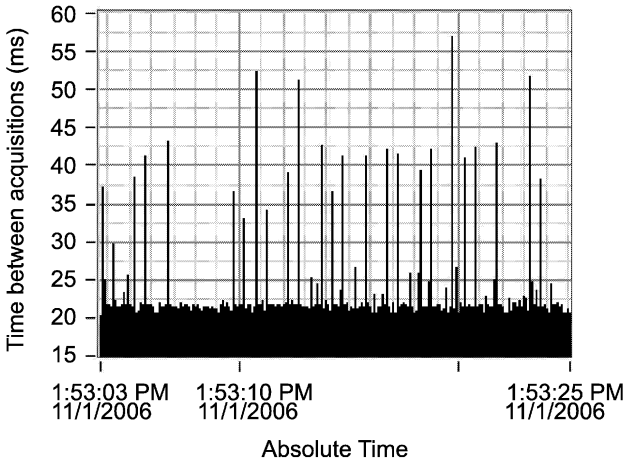

FIG. 5.—Typical performance of the acquisition and data recording for mode 3 of Fig. 4. The loop time is set to 20 ms, but due to overhead, it typically ranges between 20 and 22 ms, while occasional lags of up to 57 ms are seen. Mode 3 is used for daily solar observing.

or tracking the Sun, do not require new hardware and software development. The other parts that need to be controlled or monitored are the RF switches of the block down-converter, the tunable LO, the spectral-line down-converter, the digitizer, and the data-storage system. The embedded CPU in the spectral-line down-converter module provides the voltage AGC status (IF_{out} and IF_{out} attenuation), the measurement of IF total power (P_{sys}) level, and other monitor information through CAN-bus messages. The control and acquisition software is implemented in LabVIEW. There are two reasons that LabVIEW was selected as the control platform. As mentioned above, using LabVIEW's multithreaded programming, we can use separate acquisition and writing threads running in parallel in order to maximize the duty cycle. The second reason is that the graphic interface makes it easy to view intermediate observation results, such as the multichannel auto- and cross-correlation spectrum, P_{sys}, IF_{out}, and other system settings. This allows us to monitor the health of the system and locate and respond to problems quickly. Tabbed views in the interface allow a dense and complete yet well-organized display of information.

Synchronization between the FST system and the OVSA antenna control is done through intermediary "scheduling" soft-

ware running on the OVSA data analysis PC. Through the LabVIEW data socket server and client, the scheduling software controls such FST actions as setting the observing parameters and frequency-switching sequence, sending a scan description, and starting and stopping data recording.

The data are written to disk in a self-describing LabVIEW binary data format. We have written IDL software that allows this self-describing format to be read transparently by IDL—the data language that we use for all subsequent analysis. Changes to the data format at the LabVIEW level (such as additions to the file or record header structure) therefore require no changes to the IDL-reading software. The file sizes can be set within the LabVIEW acquisition program and are typically set at 100 Mbytes each. In our typical solar observing mode (mode 3 of Fig. 4), each file contains 6–7 s of data and are composed of a file header containing information that cannot change within the file, followed by a series of data records. Each data record represents one acquisition (which may contain multiple segments if taken in mode 2 of Fig. 4) and has a header containing information about the band, sideband, polarization state, noise diode state, and other settings pertaining to that record, followed by an array of 8 bit digitized data samples (1 signed byte per sample) for each recorded channel. The data samples are to be later scaled to true power units by the application of the measured $P_{\rm sys}$ recorded in each record header.

2.6. Software Correlator

The recorded data are processed offline using FOCIS (FASR Offline Correlator Implemented in Software). A block diagram for the flow of the processing is shown in Figure 6. A key advantage of recording the full-resolution digital data and processing them offline is that we can process the data in different ways (e.g., with different levels of bit-sampling, frequency channelization methods, RFI excision algorithms, frequency and time averaging, and correlation) in order to simulate and test hardware implementations for the future FASR digital system. This test bed function is the main goal of FST and also provides rich data sets for side-by-side comparison of RFI excision algorithms, calibration approaches, and optimum tradeoffs of time and frequency resolution with signal-to-noise ratio for solar bursts.

The software correlator, written in IDL, allows the setting of key parameters at run time, such as the number of time samples in each block (which sets the frequency resolution), the integration time (number of blocks to accumulate), and whether to apply amplitude and/or phase corrections. Other functions are controlled internally by selecting "plug in" modules for frequency channelization (fast Fourier transform [FFT] or polyphase filter, for example), with different windowing functions or digital filter coefficients, and different modules for RFI excision.

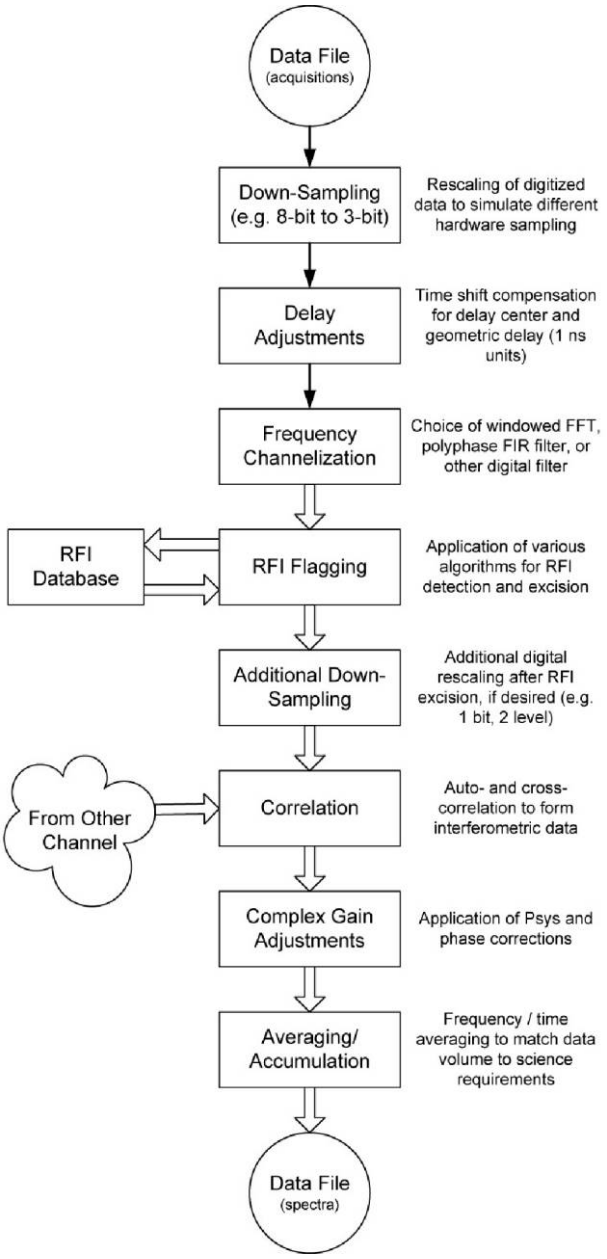

FIG. 6.—Block diagram for a single channel of the offline software correlator FOCIS. The fact that the full time-resolution waveforms are recorded allows us to run FOCIS repeatedly with different parameters and function blocks to simulate any hardware implementation.

2.7. Calibration

For FST, the small number (three) of small-diameter antennas (1.8 m) precludes the direct use of cosmic sources for calibration. However, the same antennas are used in the OVSA array, for which we have baselines involving the 27 m antennas. Therefore, it is possible to transfer the OVSA calibration as follows. We observe cosmic sources, such as 3C 84, with the

OVSA array to determine the antenna-based amplitude and phase calibration for antennas 5, 6, and 7. We then observe solar bursts and the stronger active regions with both OVSA and FST. The OVSA baseline-based amplitudes and phases are compared with those measured by FST on the same baselines, and the FST amplitudes and phases are corrected to agree with those from OVSA. To do this accurately requires using only those frequencies of the FST band that correspond with the smaller bandwidth of OVSA. This technique yields a band-averaged complex gain correction, but does not allow a bandpass calibration. A general procedure for transferring the OVSA calibration to FST in this way is still under development.

The absolute flux calibration is done by referencing the measured flux to tabulated solar flux values available from other radiometers. A bandpass amplitude calibration is first carried out through the intermediary of an injected "cal" source (noise diode [nd]) at the front end, which is used as a secondary calibration source. The procedure is to observe the blank sky (in both right and left circular polarization [RCP and LCP, respectively]), alternately turning the noise diode on and off. This yields the quantities $T_{\rm sky\,1}$ and $T_{\rm sky\,1} + T_{\rm nd\,1}$, the difference of which provides $T_{\rm nd\,1}$. We then point the antennas at Sun center and repeat the measurement, yielding the quantities $T_{\rm sky\,2} + T_{\rm Sun}$ and $T_{\rm sky\,2} + T_{\rm Sun} + T_{\rm nd\,2}$, the difference of which provides $T_{\rm nd\,2}$. The contribution of the Sun to the system temperature is $T_{\rm sys} = T_{\rm cal}[(T_{\rm Sun} + T_{\rm sky\,2})/T_{\rm nd\,2} - T_{\rm sky\,1}/T_{\rm nd\,1}]$ K, where $T_{\rm cal}$ is the noise diode temperature. This is related to the flux density of the Sun through the well-known relation $S = 2kT_{\rm sys}/\eta A$, where A is the antenna area and η is a frequency-dependent efficiency factor less than unity. To the extent that η and the noise diode temperature (~1200 K) are known, this procedure yields the solar flux density directly. The profile shown by the solid line in Figure 7 shows the antenna temperature for one particular day on one antenna. The calibrated data can be compared with measurements at specific frequencies in the FST band taken by the US Air Force Radio Solar Telescope Network, radiometers at Penticton (Canada) and Nobeyama (Japan), and with the known shape of the quiet-Sun temperature spectrum (Zirin et al. 1991). The dotted curve in Figure 7 shows such a comparison for one particular day when the Sun was quiet. The curve was derived from the quiet-Sun flux density for that date, given by the NOAA Space Environment Center, assuming $T_{\rm cal} = 1200$ K and $\eta = 0.6$. The noise diode calibration procedure results in remarkably continuous total power spectra, with antenna temperature contributions close to what we expect. Some small ripples remain in the spectrum, largely due to variations in antenna efficiency and noise diode coupling into the system. Such variations are removed by assuming smoothness in the solar spectrum.

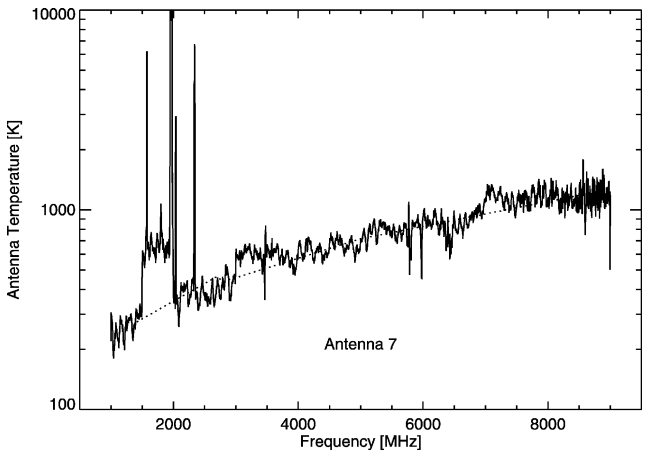

FIG. 7.—Total power spectrum of the Sun on 2006 August 31, measured as antenna temperature (on OVSA antenna 7) in RCP, and calibrated by injecting a noise diode of assumed temperature $T_{\rm cal} = 1200$ K into the signal path. For comparison, the dotted line shows the antenna temperature contribution deduced from the quiet-Sun flux spectrum tabulated by NOAA Space Environment Center for the same day. Prominent narrow interference features are visible across the spectrum; the band between 1.5 and 2.0 GHz is dominated by a very broad and strong interference line at 1.96 GHz that causes nonlinearity and hence does not calibrate well.

2.8. Daily Operation

Since about 2006 June, the FST has been operating daily in solar observing mode targeting solar bursts, while doing special observations, such as RFI surveys and satellite observations, as needed. Due to the huge volume of data, the daily observation of solar bursts requires careful coordination, as follows. A typical day's observations take up about 300 Gbytes of storage, while the data-recording PC has a total storage of 500 Gbytes. Therefore, at the end of each day's observing, an automated procedure must determine the periods of likely solar activity and delete all data outside of those periods. Because OVSA is observing in parallel and has a solar burst monitor providing a record of periods of radio burst activity, we examine the OVSA flare file and keep all periods flagged as flare periods. We also examine the daily solar event list provided by NOAA's Space Environment Center and keep other periods as appropriate. We have found that the FST data themselves are not reliable indicators of solar bursts, due to variable RFI and other variations that may swamp the weaker bursts. Because we are in a solar minimum, solar bursts are relatively rare, so on most days we keep no data at all, except for the integrated $P_{\rm sys}$ records. On some days, however, we may save as much as 10%–20% (30–60 GB) and transfer it to an external hard disk via USB (universal serial bus). When the external hard disk is full, we ship it from the Owens Valley Radio Observatory (OVRO) site in California to the New Jersey Institute of Technology, where we inspect the data visually and pare it down to a typically much smaller volume for permanent storage and further analysis. The data to be saved are transferred off the external disk, and the disk is returned to OVRO for reuse.

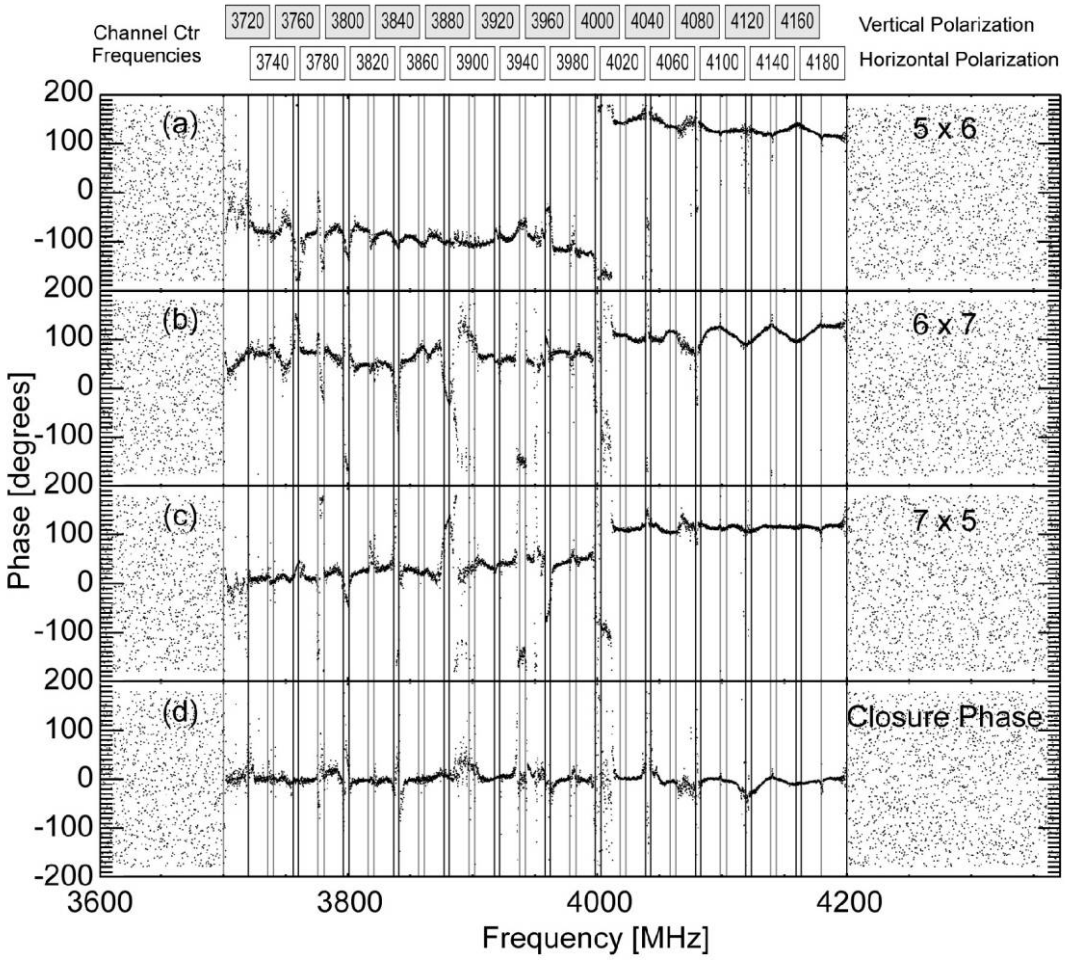

FIG. 8.—Correlated phase on all three baselines (*a–c*) and closure phase (*d*) on geosynchronous satellite *Galaxy 10R*, as measured in two 500 MHz bands of FST. Phases outside the signal band (3700–4200 MHz) are random. Phases within the signal band vary within the 24 overlapping channels of the satellite, which are shown schematically by rectangles above the plot. Channel-center frequencies are given in each rectangle, and the channels shown by gray rectangles are vertically polarized, while the channels shown in white are horizontally polarized. Vertical lines show the channel edges, to guide the eye.

3. OBSERVATIONAL RESULTS

3.1. Observation of Geosynchronous Satellites

First fringes with FST were obtained on a GPS satellite in early 2006 March, which allowed a rough determination of the phase center of the system. A more precise determination was made by tracking the geosynchronous satellite *Galaxy 10R* at local coordinates h.a. = 5.359°, decl. = −5.897°, on 2006 March 14. Three 2 ms acquisitions were taken in each of two bands, 3500–4000 and 4000–4500 MHz, encompassing the C-band transmission range of the satellite. Figure 8 shows the cross-correlation phase on each of the baselines (5–6, 6–7, and 7–5), and the closure phase, after vector averaging the three acquisitions. The analysis was done with 10,000-sample blocks, yielding a frequency resolution of 100 kHz.

This broad range of transmitted frequencies (3700–4200 MHz) is useful for determining delay centers. The delay centers applied in Figure 8, using antenna 7 as the reference antenna, are 0, 959, and 0 ns for antennas 5, 6, and 7, respectively. It is obvious that these delay center values result in a relatively flat phase variation versus frequency. A further change of 1 ns causes worse phase slopes, so the delay centers can be taken as 0, 959, and 0 ns to within the 1 ns resolution of the 1 Gsps digitizer. Note that there is a phase jump from one FST band to another (on either side of 4000 MHz), which is expected due to a change in system phase, uncorrected in Figure 8. Note also that the antenna 5 delay center is 0 ns (relative to antenna 7), which shows that our matched fiber lengths and other cable and electrical lengths in the system are precisely equal. The lengths were matched purposely (§ 2.1) in order to investigate the effects of thermal variations on the phase. Thermal variations in the fiber will affect baselines involving antenna 6 but should be absent on baseline 7–5.

Some smooth phase deviations across the band in Figure 8 could be variations in complex gain over the band, but other variations and abrupt jumps are clearly associated with the broadcast channels of the satellite. The C-band channel distribution for *Galaxy 10R* is shown at the top of Figure 8. The channels are distributed with overlapping channels in *V* and *H* linear polarizations. The closure phase (Fig. 8, *bottom*), should be zero for all geometrically defined phases, and while the overall trend is flat at zero, there are clearly significant deviations due to the character of the signals on the channels. The residual phase variations in Figure 8, particularly the nonzero closure phase, can be attributed to the fact that there is more than one satellite in the primary beam (2.9° half-power beamwidth) of the 1.8 m antenna. The geosynchronous stations over the US are fully used and are separated by 2° or less, which makes the use of geosynchronous satellites problematic for phase calibration of small antennas.

The geosynchronous satellites sometimes have "beacon" frequencies that are useful for phase and frequency calibration. *Galaxy 10R* is a PanAmSat satellite whose beacon frequencies are at 4.198125 and 4.199625 GHz. These beacon signals are easily seen in the data at a frequency resolution of 100 kHz, as shown in Figure 9*a*. To check the FST frequency calibration, we reanalyzed the data using 100,000-point blocks, for a 10 kHz frequency resolution. Figure 9*b* shows that the line at 4.199625 GHz appears at precisely the correct frequency as expected.

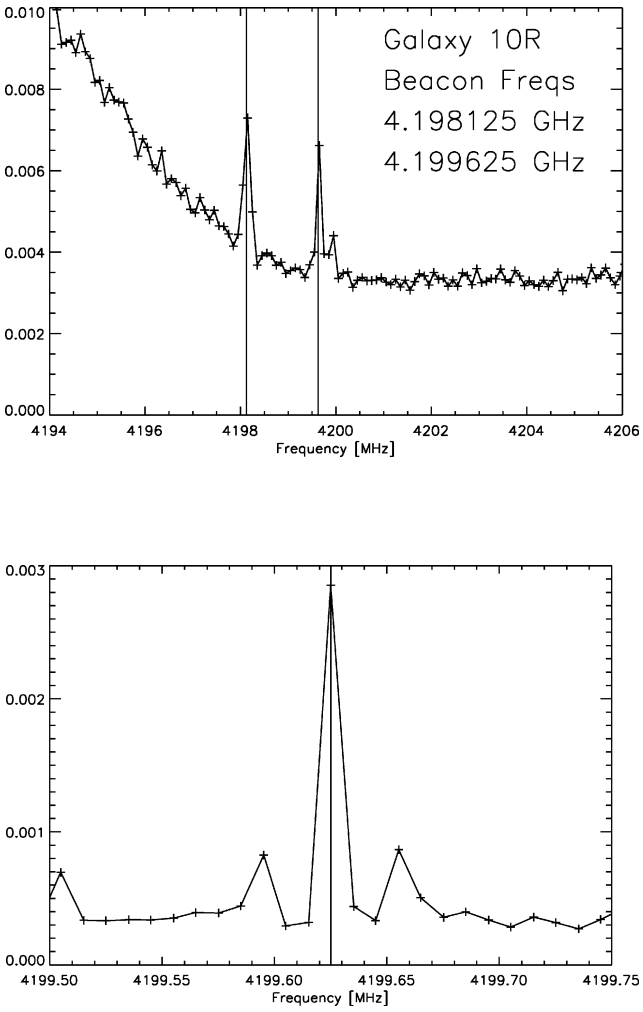

FIG. 9.—*Top*: Beacons for geosynchronous satellite *Galaxy 10R*, overlaid with vertical markers showing the nominal frequencies of the lines. These beacons are *V* polarized. The vertical axis is total power in arbitrary units. *Bottom*: Upper frequency beacon at 10 kHz resolution, overlaid with a vertical marker showing the nominal frequency of the line. The line is symmetrically centered on the marker, confirming that FST frequency calibration is precisely correct to within a small fraction of 10 kHz. The vertical axis is total power in arbitrary units.

3.2. Observation of GPS Satellites

GPS satellite *22779* was tracked starting at 14:26 UT on 2006 April 21, using a position calculated from the standard "two-line elements" (TLE) data from NORAD (North American Aerospace Defense Command). The GPS L1 signal is centered at 1.57542 GHz and spans a 10 MHz bandwidth, due to the satellite's P-code modulation. Figure 10 shows the correlated phase as a function of frequency using the delay centers of 0, 959, and 0 ns found previously. The phase is relatively flat over the 10 MHz band of the L1 signal, except at frequencies with non-GPS interference at 1576 and 1577 MHz. Figure 11 gives the correlated phase as a function of time over about 28 minutes at 1574.5 MHz. The analysis was done with 1000-point blocks, yielding 1 MHz resolution. The left column shows the phase for the three baselines and closure phase, before geometric phase correction. Note the rapid phase wind in the three channels, while the closure phase remains zero.

The rapid phase rotation is due to applying the geometrical delay to the IF (0–500 MHz) digitized data instead of in the RF signal path, where the delay actually occurs (Thompson et al. 2001). The correction for this phase variation is called "fringe stopping" and depends on the various stages of downconversion in the FST system. The Appendix gives a derivation of the general equation for the phase correction, which is

$$\phi = (\sigma\omega_{\rm BL} - \sigma\omega_{\rm LO} - \omega_D)\tau_g - \sigma\omega_{\rm RF}\tau_c, \qquad (2)$$

where τ_g is the geometric delay, $\omega_{\rm BL}$ is the angular frequency of the block down-converter ($2\pi \times 10$ GHz), $\omega_{\rm LO}$ is the angular frequency of the LO, ω_D is the angular frequency of the digitizer down-conversion (2π GHz), and σ is -1 for lower sideband and $+1$ for upper sideband. However, an additional phase correction is needed, due to the fact that the delays are implemented by shifting the digital data on each channel by an integral number of 1 ns samples, as discussed in § 3.1. The combined phase correction is obtained by replacing the true

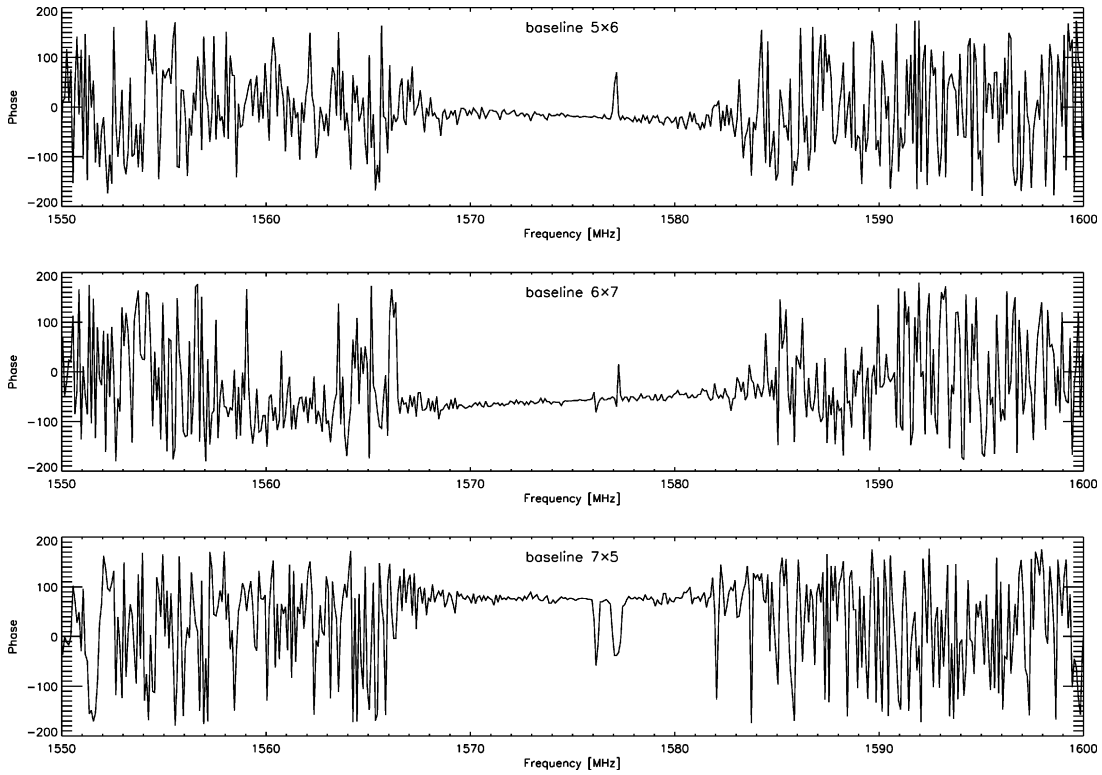

FIG. 10.—GPS satellite phases vs. frequency for the three baselines. Note that the phases across the 10 MHz band centered at the L1 frequency 1575.27 MHz are flat. Also note that there is interference at 1576 and 1577 MHz.

delay τ_g by the integer delay $\tau_1 = \text{round}(\tau_g)$ and applying a frequency-dependent term proportional to the noninteger part of the delay, $\delta = (\tau_1 - \tau_g)$:

$$\phi = (\sigma\omega_{\rm BL} - \sigma\omega_{\rm LO} - \omega_D)\tau_1 \pm \sigma\omega_{\rm RF}\delta. \quad (3)$$

Here the upper sign is for an IF in the 1–5 GHz band, and the lower sign is for the 5–9 GHz band, and $\omega_{\rm RF}$ is the RF angular frequency ($2\pi f_{\rm GHz}$). This calculated phase must be subtracted from the raw phase.

The middle column of Figure 11 shows the phase of the three baselines and closure phase after the above phase correction. Note that the phases are nearly flat, but the baselines involving antenna 6 (*top two rows*) are still drifting significantly with time over the 28 minute observation. We interpret this as being due to a limitation on the precision of orbital positions provided by the TLE-derived coordinates (e.g., Chan & Navarro 2001). A best-fit determination of the error between the phase center (TLE-derived coordinates) and the position of the satellite is 4.81′ in hour angle and 6.39′ in declination. After correction for this phase center offset, the phases are nearly constant over the observation, as shown in the right column of the Figure 11 plots. Similar observations with other satellites indicate a typical error of an order of 10′. Unfortunately, such a large error precludes the use of GPS satellites as absolute phase calibrators when TLE data are used to determine the satellite position.

3.3. RFI Mitigation

One of the main goals of FST is to provide a unique test bed for studying methods of RFI excision. RFI is observed as being present in virtually every one of our bands, and the high time and frequency resolution provided by FST allows us to characterize it in great detail. We are using the daily solar data to quantify the occupancy statistics of RFI for the OVRO site. We are also exploring the use of time-domain kurtosis (Kenney & Keeping 1962), in addition to a variant of the kurtosis method in the frequency domain, to identify the presence of RFI and thus flag bad channels in simulated real time (i.e., we play back the raw, full-resolution recorded data and flag the bad channels during playback, just as a real-time system would do). The ability to select alternate RFI excision algorithms during playback allows us to compare algorithms on an equal basis. Further details are to be presented in another paper (Nita et al. 2007).

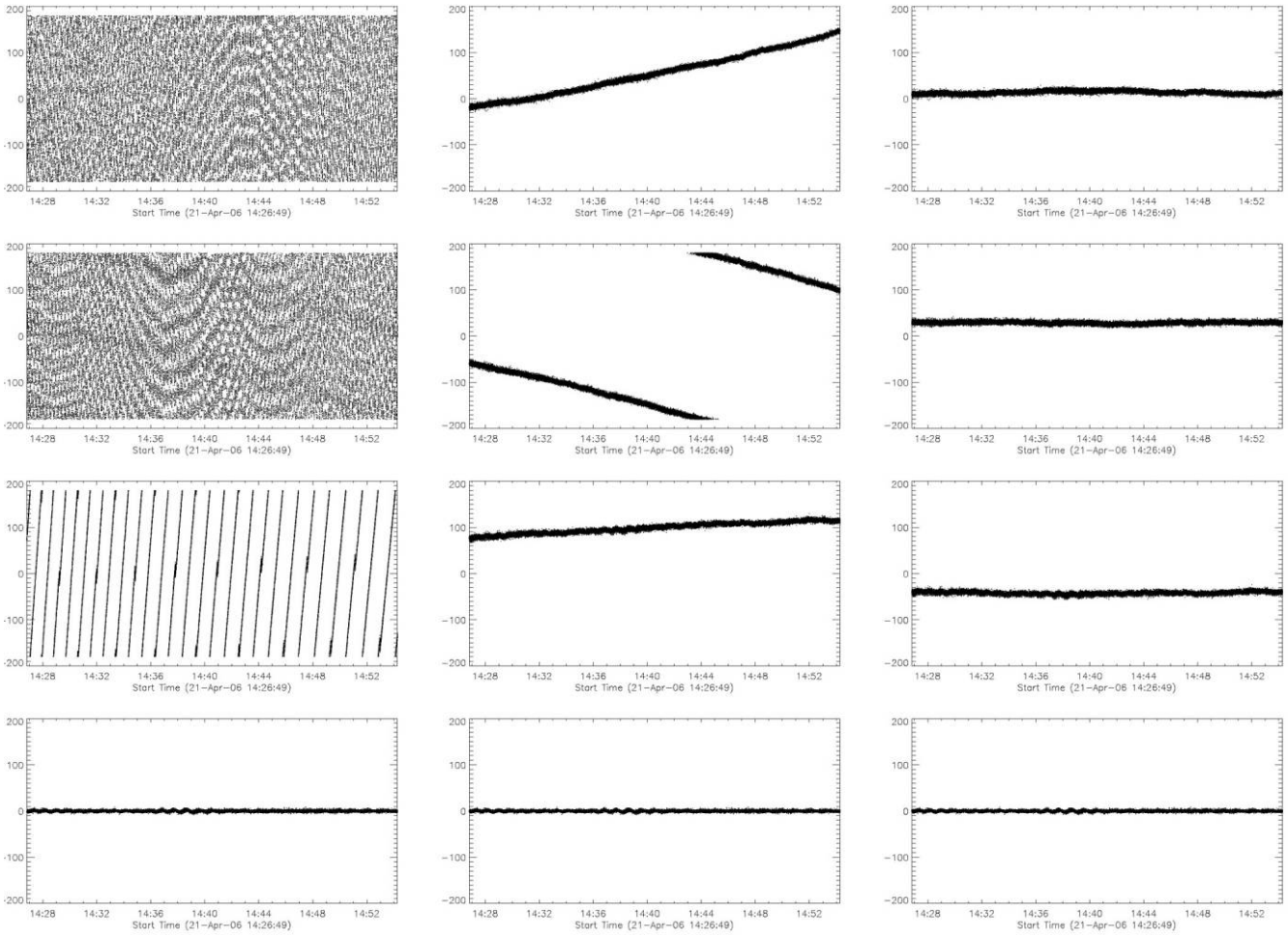

FIG. 11.—Correlated phases (*left to right*) for three baselines and closure phases (*top to bottom*). *Left*: raw phase; *middle*: phase corrected for fringe-stopping correction; and *right*: phases with fringe-stopping and refined estimate for satellite location.

3.4. Observations of Solar Bursts

Type III solar bursts are due to beams of electrons traveling upward and downward in the solar corona at speeds as high as 0.5*c*. Type III burst emission is generated at the local plasma frequency or its second harmonic. Since the plasma frequency is proportional to the square root of coronal electron density, one can estimate the height of the emission by assuming a coronal density model (e.g., Newkirk 1961). Combined with interferometric observations, this provides the ability to locate and track such sources in three dimensions.

Various authors have given the frequency drift rate of type III bursts at different frequencies (Stahli & Benz 1987 [8.1 ± 4.3 GHz s^{-1} at 3.47 GHz]; Allaart et al. 1990 [11 ± 9 GHz s^{-1} at 6.0 GHz]; Benz et al. 1992 [11.5 ± 8.5 GHz s^{-1} at 7.5 GHz]). In addition, the relation between duration, drift rate (in MHz s^{-1}), and observing frequency for the decimetric range (0.3–3.0 GHz) has been found to be

$$t_{1/2} = 1.7 \times 10^4 f^{-0.60}, \tag{4}$$

$$|df/dt| = (0.09 \pm 0.03) f^{1.35 \pm 0.10} \tag{5}$$

(Melendez et al. 1999), where $t_{1/2}$ is the half-power duration in ms, and f is in MHz. The half-power duration ranges between 139 and 269 ms in the overlapping FST frequency range (1–3 GHz). This duration suggests that we must use either mode 2 or mode 3 of Figure 4, both of which have 20–25 ms between acquisitions, appropriate for resolving the bursts. After initial observations in mode 2, we have settled on mode 3 as the optimum choice, due to its elimination of the data-transfer time gap, coupled with the fact that we do not require a precise time

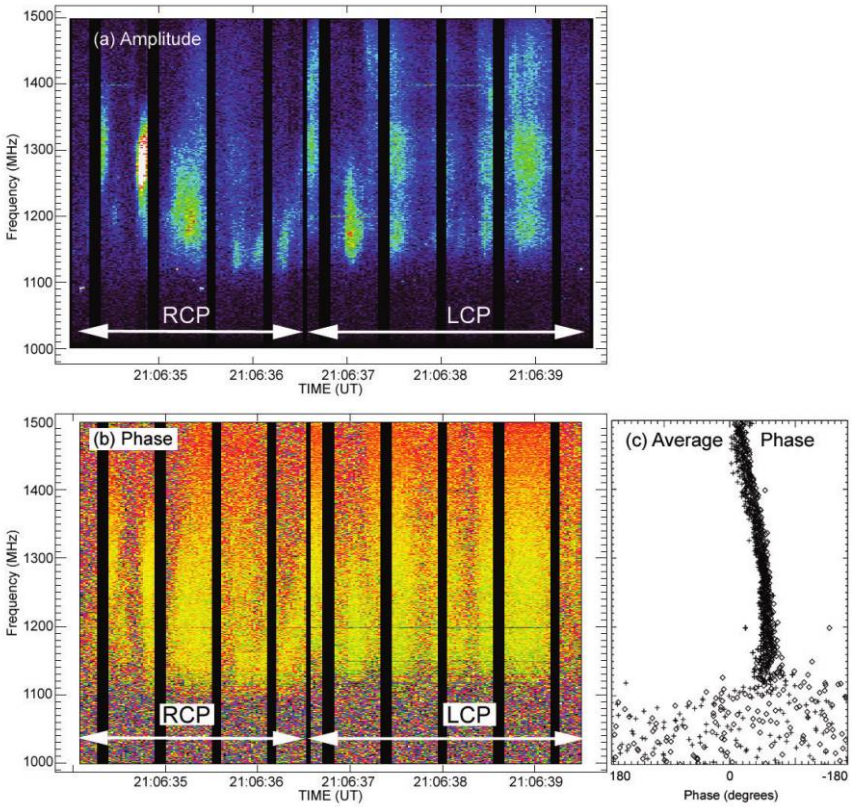

FIG. 12.—Correlated amplitude (*a*) and phase (*b*) of a type IIIdm burst with reverse drift indicative of downward-going electron beams. The phases are relative to the preflare (active region plus system phase). The polarization changes from RCP to LCP at the point shown, but the phases are unchanged, indicating that both polarizations arise from the same location to within about 10″. This suggests a low degree of polarization, as expected for second-harmonic plasma emission. (*c*) Plot of phase from a vector average of the data in (*a*) and (*b*), averaged separately for RCP (*plus symbols*) and LCP (*diamonds*).

interval between acquisitions. The ability of FST to measure phase (and hence positions) in two dimensions as a function of frequency should allow each type III burst's trajectory to be traced. Because FST can measure only one 500 MHz band at a time, and in a single polarization, we decided to take data in the lowest frequency band (1–1.5 GHz) and to switch polarization alternately every few seconds. We have used this setup exclusively for our daily solar observations until recently (2006 November) to maximize the chance to observe type III bursts, which are most numerous at lower frequencies and may be highly polarized in either sense of circular polarization.

The first burst seen by the FST system, associated with a B5.1 X-ray class flare, was recorded in mode 2 at 20:30 UT on 2006 April 5. Figure 12 shows the correlated dynamic spectrum in both amplitude and phase. The gaps between the spectrum strips are due to the dump time between acquisitions (see Fig. 4). The dynamic spectrum shows the presence of several type III bursts, some of which show a clear reverse-drift behavior (drifting from low to high frequencies). That indicates the event is a type III burst generated by downward-going electron beams. The duration of individual bursts is ~175 ms, and the drift rate is 700 MHz s^{-1}, which are consistent with the above empirical relations for type III burst duration and drift rate in the decimetric range (Melendez et al. 1999). A full study of this event is under way, but one can immediately see from Figure 12*b* that all of the individual type III bursts have precisely the same phase behavior, whether seen in right or left circular polarization. This implies that each burst follows the same trajectory (at least in the one dimension measured by the single baseline) within the roughly 10″ spatial resolution of the observation.

Since that first event, we have recorded 11 additional events, including two bursts of soft–X-ray class X. The event of 2006 August 31, a mere B7.0 X-ray class event, proved to be extremely strong and rich, lasting nearly 2 hr and showing spike bursts (Bastian et al. 1998), weak type III bursts, fiber bursts (Kuijpers & Slottje 1976; Aurass et al. 2005), and strong continuum activity. Figure 13 presents a short 30 s period during the burst, showing fiber burst activity. This burst promises to provide the first spatially resolved observations of these enigmatic drifting bursts. The radio diagnostics available from the high time and frequency resolution FST data, coupled with

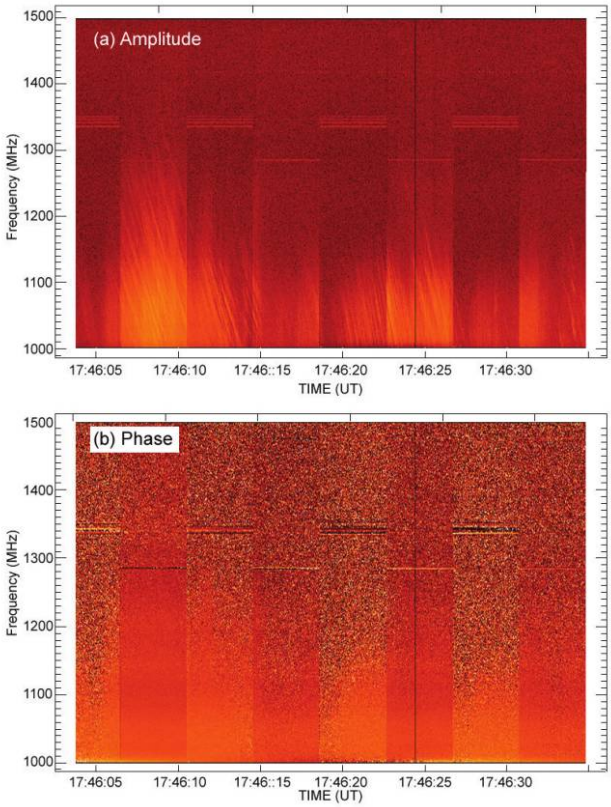

FIG. 13.—Correlated amplitude and phase for a short period (30 s) of a long-lasting (nearly 2 hr) type IV continuum solar burst, with fiber bursts superimposed. This is a period of emission in both RCP and LCP, although most of the burst was essentially 100% LCP. The fiber bursts are the prominent features, each drifting from as high as 1300 MHz to the low-frequency limit of 1000 MHz over about 3–4 s. There is little phase (i.e., position) difference between the type IV continuum source and the fiber burst emission, but more careful study is under way to determine both the continuum and fiber burst locations as a function of frequency.

the unique interferometric spatial information, are a powerful combination provided by this FASR prototype instrument, which shows a small part of the capability of the complete FASR.

4. CONCLUSIONS

The architecture of the FASR Subsystem Testbed has been described. For the first time, it provides the capability to observe the Sun with three-dimensional (temporal, spectral, and spatial) information simultaneously for a broad bandwidth (500 MHz). As a prototype for FASR, FST also provides the opportunity to study the design, calibration, and interference-mitigation requirements of FASR. Since the correlated spectra are derived through offline software from full-resolution data, FST provides the flexibility to process the data multiple times with alternate algorithms and parameters in order to simulate various hardware designs using real data. It is this unique capability that makes FST so valuable as a test bed instrument. In addition, FST observations provide an excellent database for testing RFI mitigation algorithms under the real-world conditions we might expect for FASR.

The initial observational results demonstrate the extent to which satellite observations can be exploited to calibrate the system. Observations of geosynchronous satellites provide precise determination of the delay center, frequency calibration, and relative phase calibration, but neither geosynchronous nor GPS satellites are suitable for absolute phase calibration, unless their positions are better known than those calculated from the NORAD two-line element sets. All observations and tests show that FST performs its expected function extremely well. Several solar bursts captured by the FST system nicely demonstrate the promise of FST, and hence that of the future FASR, for further solar observations. The instrument will continue daily solar observations, with the expectation that it will allow us to trace type III electron trajectories and also locate the source positions of other decimetric bursts that are applicable to the height range in which the primary energy release of solar flares is expected to take place. The huge amount of raw data makes the daily operation a rather challenging data management problem, and our operations model will break down during solar maximum when flares are more numerous, unless we do more extreme data selection. A number of studies are under way using the first 6 months of data from the instrument, and we look forward to continued observations in the future.

We thank Brad W. Wiitala from Caltech, who designed the spectral-line down-converter. We also thank Kjell Nelin for help with the observations. David Woody and David Hawkins at OVRO are also acknowledged for helpful discussions. This research was supported by NSF grants AST 03-52915 and AST 06-07544, and NASA grant NNG 06GJ40G to the New Jersey Institute of Technology.

APPENDIX A

PHASE CORRECTION

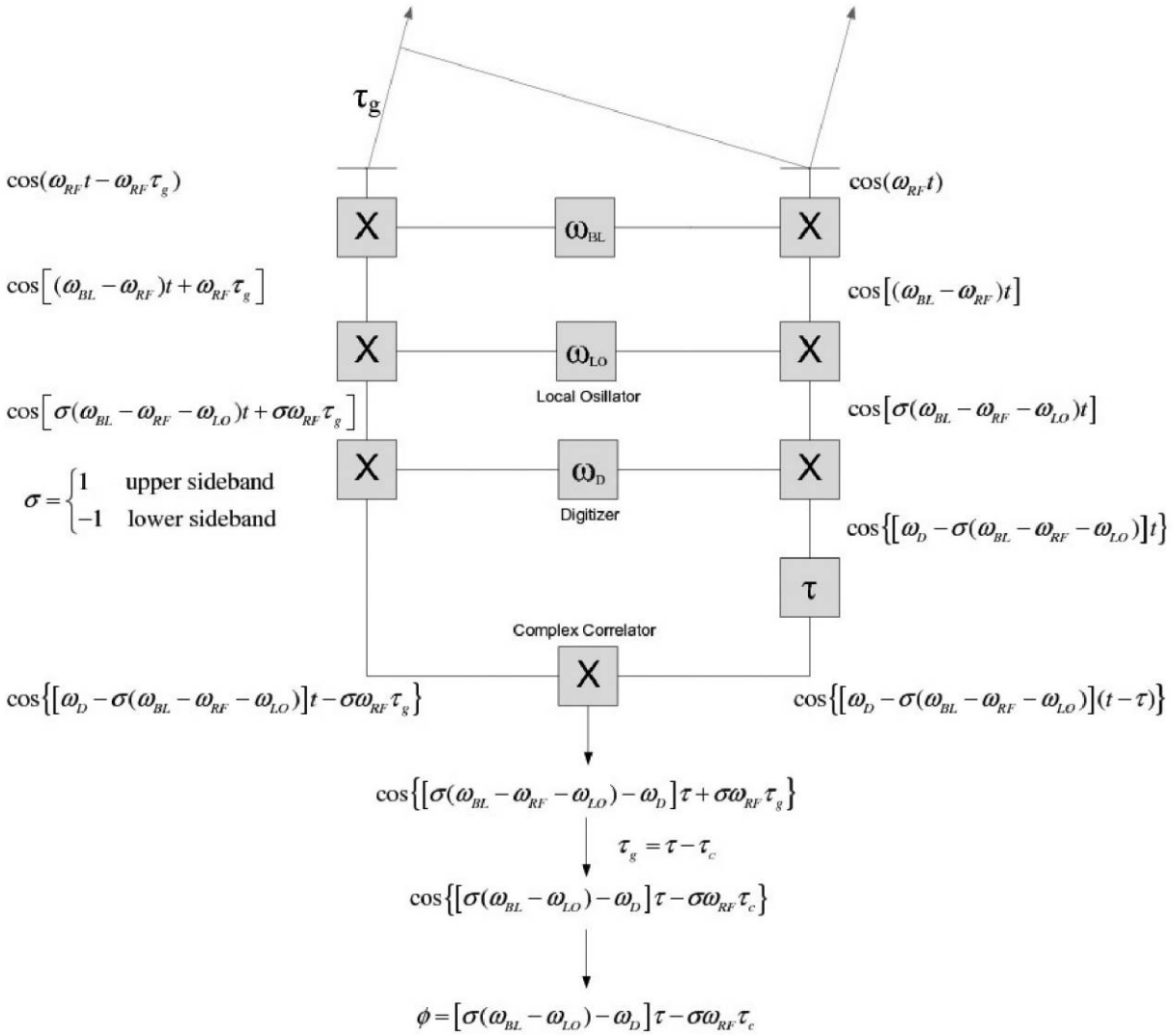

FIG. 14.—Origin of the phase correction needed due to two stages of explicit down-conversion and one stage of implicit down-conversion due to the digitizer. See Appendix for details.

The FST uses two explicit levels of down-conversion, plus one additional implicit down-conversion by the digitizer. The down-conversions introduce phase rotation (natural fringes) at the LO frequency. The general expression is developed here and given in equation (2). Figure 14 provides a schematic view of a single baseline, in which the incoming wave front of frequency $\omega_{\rm RF}$ arrives at one of the antennas after some geometric delay τ_g that depends on the baseline length and the direction to the source. To compensate for this delay, a delay $\tau = \tau_g + \tau_c$ is introduced in the other antenna just prior to correlation, where τ_c is a time- and frequency-independent delay (called the delay center) that takes into account unequal cabling and other system delays not related to the source-baseline geometry. At the antennas, the time-dependent voltages have the dependencies $\cos(\omega_{\rm RF}t)$ and $\cos(\omega_{\rm RF}t - \omega_{\rm RF}\tau_g)$. We ignore any additional antenna-based phase shifts, which are corrected during calibration. After the first down-conversion (at block–down-

converter frequency $\omega_{\rm BL}$), the voltages are proportional to $\cos[(\omega_{\rm BL} - \omega_{\rm RF})t]$ and $\cos[(\omega_{\rm BL} - \omega_{\rm RF})t - \omega_{\rm RF}\tau_g]$. Here

$$\omega_{\rm BL} = \begin{cases} 2\pi f_{\rm BL}, & \text{upper band,} \\ 0, & \text{lower band,} \end{cases} \tag{A1}$$

where $f_{\rm BL} = 10$ GHz. Likewise, after a second stage of down-conversion (at variable-LO frequency $\omega_{\rm LO}$) within the spectral-line down-converter modules, the voltages are proportional to $\cos[\sigma(\omega_{\rm BL} - \omega_{\rm RF} - \omega_{\rm LO})t]$ and $\cos[\sigma(\omega_{\rm BL} - \omega_{\rm RF} - \omega_{\rm LO})t - \sigma\omega_{\rm RF}\tau_g]$, where we have introduced

$$\sigma = \begin{cases} +1, & \text{upper sideband,} \\ -1, & \text{lower sideband,} \end{cases} \tag{A2}$$

to account for the selection of the sideband. Finally, the selected 500–1000 MHz IF is digitized at 1 Gsps, which is below the Nyquist frequency; hence, there is a further implicit down-conversion at frequency $\omega_D = 2\pi f_D = 2\pi(1\ \text{GHz})$, after which the voltages are proportional to $\cos\{[\omega_D - \sigma(\omega_{\rm BL} - \omega_{\rm RF} - \omega_{\rm LO})]t\}$ and $\cos\{[\omega_D - \sigma(\omega_{\rm BL} - \omega_{\rm RF} - \omega_{\rm LO})]t - \sigma\omega_{\rm RF}\tau_g\}$. These voltage waveforms are the raw data that are recorded by the FST system.

In the software correlator, the first channel is then further delayed by $\tau = \tau_g + \tau_c$, resulting in the final voltage waveform $\cos[\omega_D - \sigma(\omega_{\rm BL} - \omega_{\rm RF} - \omega_{\rm LO})(t - \tau)]$ for that antenna. These signals are then correlated (multiplied and integrated), removing the dependence on t, but there remains the time- and frequency-dependent phase shift $\phi = [\sigma(\omega_{\rm BL} - \omega_{\rm RF} - \omega_{\rm LO}) - \omega_D]\tau + \sigma\omega_{\rm RF}\tau_g$. Replacing τ_g with $\tau - \tau_c$, the terms involving $\sigma\omega_{\rm RF}\tau$ cancel, yielding the expression

$$\phi = [\sigma(\omega_{\rm BL} - \omega_{\rm LO}) - \omega_D]\tau - \sigma\omega_{\rm RF}\tau_c. \tag{A3}$$

This expression becomes equation (2) on replacing τ with $\tau_g + \tau_c$ and ignoring the constant term $[\sigma(\omega_{\rm BL} - \omega_{\rm LO}) - \omega_D]\tau_c$ (which becomes part of the complex gain correction, to be removed through calibration).

REFERENCES

Allaart, M. A. F., van Nieuwkoop, Slottje, C., & Sondaar, L. H. 1990, Sol. Phys., 130, 183

Aurass, H., Rausche, G., Mann, G., & Hofmann, A. 2005, A&A, 435, 1137

Bastian, T. S. 2003, Proc. SPIE, 4853, 98

Bastian, T. S., Benz, A. O., & Gary, D. E. 1998, ARA&A, 36, 131

Bastian, T. S., Bradley, R., White, S., & Mastrantonio, E. 2005, AGU Abstr. Spring, A16

Benz, A. O., Magun, A., Stehling, W., & Su, H. 1992, Sol. Phys., 141, 335

Bock, D. C.-J., et al. 2006, Proc. SPIE, 6267, 2006

Bogod, V. M., Garaimov, V. I., Komar, N. P., & Korzhavin, A. N. 1999, in 9th European Meeting on Solar Physics, Magnetic Fields and Solar Processes, ed. A. Wilson (ESA SP-448; Noordwijk: ESA), 1253

Chan, J. C., & Navarro, D. 2001, in Proc. Third European Conference on Space Debris, ed. H. Sawaya-Lacoste (ESA SP-473; Noordwijk: ESA), 771

DeBoer, D. R., et al. 2004, Proc. SPIE, 5489, 1021

Gary, D. E., & Hurford, G. J. 1999, in Proc. Nobeyama Symp., Solar Physics with Radio Observations, ed. T. S. Bastian, N. Gopalswamy, & K. Shibasaki (NEO Rep. 479; Tokyo: Nobeyama Radio Obs.), 429

Gary, D. E., & Keller, C. U., ed. 2004, Solar and Space Weather Radiophysics: Current Status and Future Developments (Kluwer: Dordrecht)

Hartley, R., Single-Sideband Modulation, US Patent 1,666,206, issued April 1928

Hurford, G. J., Read, R. B., & Zirin, H. 1984, Sol. Phys., 94, 413

Kenney, J. F., & Keeping, E. S. 1962, Mathematics of Statistics (3rd ed.; Princeton, NJ: Van Nostrand)

Kerdraon, A., & Delouis, J.-M. 1997, in Coronal Physics from Radio and Space Observations, ed. G. Trottet (Berlin: Springer), 192

Kuijpers, J., & Slottje, C. 1976, Sol. Phys., 46, 247

Lecacheux, A. 2000, in Radio Astronomy at Long Wavelengths, ed. R. G. Stone et al. (Geophys. Monog. 119; Washington: AGU), 321

Melendez, J. L., Sawant, H. S., Fernandes, F. C. R., & Benz, A. O. 1999, Sol. Phys., 187, 77

Messmer, P., Benz, A. O., & Monstein, C. 1999, Sol. Phys., 187, 335

Nakajima, H., et al. 1994, Proc. IEEE, 82, 705

Napier, P. J., Thompson, A. R., & Ekers, R. D. 1983, Proc. IEEE, 71, 1295

Newkirk, G. J. 1961, ApJ, 133, 983

Nita, G. M., Gary, D. E., Liu, Z., Hurford, G. J., & White, S. M. 2007, PASP, in preparation

Prestage, N. P., Luckhurst, R. G., Paterson, B. R., Bevins, C. S., & Yuile, C. G. 1994, Sol. Phys., 150, 393

Stahli, M., & Benz, A. O. 1987, A&A, 175, 271

Thompson, A. R., Moran, J. M., & Swenson, G. W., Jr. 2001, Interferometry and Synthesis in Radio Astronomy (2nd ed.; New York: Wiley)

Zirin, H., Baumert, B. M., & Hurford, G. J. 1991, ApJ, 370, 779